Green Chemistry

ROYAL SOCIETY OF CHEMISTRY

PAPER

View Article Online
View Journal | View Issue

Cite this: *Green Chem.*, 2024, **26**, 2874

Supporting critical raw material circularity – upcycling graphite from waste LIBs to Zn–air batteries†

Reio Praats,[a] Alexander Chernyaev,[b] Jani Sainio,[c] Mari Lundström,[b] Ivar Kruusenberg[a] and Kerli Liivand *[a]

Received 7th November 2023,
Accepted 10th January 2024

DOI: 10.1039/d3gc04315k

rsc.li/greenchem

The use of Li-ion batteries (LIBs) is continuously growing, leading to a corresponding increase in the volume of end-of-life LIBs. Recycling of LIBs not only ensures the safe management of hazardous waste, but also minimizes the losses of valuable materials. While for some battery metals, such as Co, Ni, and Cu, industrial recovery processes have already been established, graphite is currently discarded as waste. This research introduces an innovative approach to create a bifunctional oxygen electrocatalyst by using the graphite waste fraction from hydrometallurgical recycling. Notably, we strategically utilized the residual metals left in the graphite fraction to achieve high electrocatalytic activity for both the ORR and OER under alkaline conditions. Our novel black mass-derived oxygen electrocatalyst was used as an air cathode catalyst in Zn–air batteries and demonstrated a high power density of 104 mW cm^{-2} with outstanding long-term stability of 80 hours. This work unlocks new opportunities for repurposing overlooked graphite waste in energy conversion and storage applications.

Introduction

Lithium-ion batteries (LIBs) have widespread uses in our everyday life, from portable devices to electric vehicles and even heavy machinery. The International Energy Agency (IEA) predicts that there will be a 40-fold increase in LIB usage from 2020 to 2040, which will correspondingly increase the volume of end-of-life batteries required to be recycled.[1] Already in 2019, around 0.2 million tons of spent LIBs (SLIBs) were globally available to be recycled.[2] Sustainably recovering secondary resources from SLIBs through recycling not only guarantees cost-effective and safe end-of-life management, but also safeguards critical materials from being lost. In addition, this process plays a crucial role in fortifying the battery value chain by recycling secondary resources and keeping them in a loop. The majority of LIB recycling pathways primarily prioritize the high recovery of cathode-active materials (Co, Ni, Li), due to their higher value.[3,4] However, it is worth noting that natural graphite (NG) holds significant importance in energy technologies and the steelmaking industry. Recognizing its potential supply risks, the European Commission classified NG as a critical raw material as early as 2011.[5] In addition, the United States has listed graphite as a critical and strategic mineral.[6] Graphite holds immense significance across various industries owing to its unique combination of metallic and non-metallic properties, excellent electrical and heat conductivity, good strength, chemical inertness, and heat tolerance up to 3600 °C.[7] All these beneficial properties lead to diverse applications of graphite in sectors such as the steel industry, aerospace and defence, electronics, transportation, construction, and renewable energy.[4,5] Therefore, it is imperative to prioritize the recycling of this critical material to ensure its sustained availability and utilization across these vital industries. In the industrial LIB recycling process, graphite is incorporated within the black mass, which is produced during the mechanical pre-treatment step, where batteries are crushed and sieved to form a mixture of small particles composed of all LIB components.[8] In the hydrometallurgical recycling of black mass, the process typically involves leaching out most of the cathode metals from the black mass. The remaining undissolved fraction, known as the leach residue, is typically treated as waste, and disposed of. The leach residue consists of graphite and other undissolved battery materials, like polymer binder, conducting agent (carbon black), current collectors (Al and Cu), and some undissolved cathode metals.[9] LIBs typically

---

[a] *National Institute of Chemical Physics and Biophysics, Akadeemia tee 23, 12618 Tallinn, Estonia. E-mail: kerli.liivand@kbfi.ee*

[b] *Department of Chemical and Metallurgical Engineering, School of Chemical Engineering, Aalto University, P.O. Box 16200, 00076 Aalto, Finland*

[c] *Department of Applied Physics, School of Science, Aalto University, P.O. Box 15100, 00076 Aalto, Finland*

† Electronic supplementary information (ESI) available. See DOI: **https://doi.org/10.1039/d3gc04315k**

contain approximately 20 wt% of graphite, which is presently not recycled or recovered. Instead, it is discarded as a waste fraction at the end of the recycling process.[4] Handling critical resources in this manner cannot be deemed sustainable or economically viable. Several research groups have demonstrated that the quality and structure of spent graphite may undergo only slight changes after its initial use in a battery, rendering it as a potentially valuable resource for the development of new batteries or other applications.[4,10–14]

The escalating energy consumption and the climate crisis have amplified focus on alternative green energy technologies, such as fuel cells and metal–air batteries.[15–17] However, these systems require active electrocatalysts to enhance the oxygen reduction reaction (ORR) and the oxygen evolution reaction (OER) taking place in these devices. Currently, expensive Pt or Pt alloys on carbon carriers and RuO_2 or IrO_2 are considered the best commercial catalysts for the ORR and the OER, respectively.[18,19] Even though noble metal-based catalysts are very efficient, their expensiveness and low durability make them commercially undesirable.[20–22] Therefore, there is urgency to develop low-cost, durable, and active multifunctional catalyst materials that can catalyse simultaneously both the ORR and OER. Some of the most promising candidates for substituting expensive noble metal-based catalysts are carbon-based materials that are co-doped with nitrogen and transition metal(s), like Fe and Co.[23–26] Furthermore, carbon-based materials are excellent catalyst supports, due to their low cost, good electrical conductivity, durable structure, resistance to acids and bases, and good adjustability.[16,20,26–28] However, the synthesis of a multifunctional catalyst material, which catalyses both reactions simultaneously, can be a great challenge due to the need for different catalytic sites and mechanisms. Pioneering work on M–N–C-type catalysts was conducted by Jasinski, who demonstrated that introducing transition metals with nitrogen into the carbon lattice through pyrolysis significantly enhances the activity of ORR electrocatalysts.[29,30] Nowadays, M–N–C-type catalysts are typically prepared by mixing nitrogen sources, high purity metal salt/oxides, and carbon materials. Subsequently, the mixture is pyrolyzed to introduce metal and nitrogen species into the carbon structure. This process leads to the formation of N–C and M–Nx-type bonds, which are recognized as active sites for the ORR and the OER.[31–38] In addition to nitrogen species, metal nanoparticles encapsulated by carbon or metal oxides are well-known OER active centres.[39–42] The ability to catalyse both oxygen reactions, good capacity, and long-term stability are required characteristics for promising bifunctional oxygen electrocatalysts that could be applied in rechargeable Zn–air batteries (ZABs) as air cathode catalyst materials.[32] Co–N–C-type catalysts have shown high peak power densities and long-term stabilities in ZABs, which make them favourable candidates to be used commercially.[39,42–48] In addition, carbon-supported multi-metallic catalyst materials, such as Co–Fe or Co–Ni, have shown promising results. However, the precise mechanism underlying the synergistic effects of multiple metals in enhancing oxygen reduction reactions (ORRs) and oxygen evolution reactions (OERs) remains unclear.[49–53] These intelligently designed materials often require multi-stage synthesis steps and expensive reagents as carbon support materials and/or metal complexes, which limit the commercialisation possibilities of these materials. To date, there have only been a few studies where recycled materials from SLIBs were used to synthesise electrocatalysts for the ORR and the OER. In most of these studies, the cathode or anode is manually extracted from the used LIB and individually processed to extract Co salt or used graphite. Yang *et al.*[54] and Bian *et al.*[55] recovered Co salt from the SLIB cathode layer to synthesize a bifunctional oxygen electrocatalyst. Graphite recovered from the anode layer has been used as a precursor material for reduced graphene oxide (rGO)-based catalyst materials.[14,56–58] Liivand *et al.* successfully synthesised a graphene-like bifunctional oxygen electrocatalyst from black mass leach residue.[58]

This research presents a novel approach utilizing the leach residue from hydrometallurgical recycling as a cost-effective raw material for oxygen electrocatalyst production. This residue, containing graphite and residual transition metals (Co, Ni, Mn, and Cu), served as a source of carbon and metals, enabling the synthesis of a highly active and stable bifunctional electrocatalyst for enhancing both the ORR and OER. Moreover, this synthesized catalyst exhibited exceptional performance as an air electrode catalyst material in rechargeable zinc–air batteries. This work aligns with the main purposes of the circular economy, reducing the waste generated from battery recycling while contributing to the development of next-generation green energy technologies.

Experimental section

Procurement of leach residue and synthesis of the catalyst material

LIBs from used laptops and mobile phones were subjected to industrial crushing, whereupon magnetic separation and sieving processes were used to generate a Co-rich black mass. Before our research, this black mass had previously undergone hydrometallurgical treatment, as reported by Chernyaev *et al.*,[59] which effectively leached out the majority of cathode metals, leaving behind the graphite-rich waste fraction. This graphite-rich leach residue was used as the starting material in this research, referred to as the raw material. The raw material consists mainly of graphite with additional impurities such as plastics (separator and binder) and traces of undissolved metals (Co, Ni, Al, Mn, Cu).[59] To synthesize the catalyst material, we used the raw material directly or subjected it to a heat treatment process to eliminate the organic impurities and binder. For the heat treatment, the raw material underwent flash pyrolysis at 800 °C for 1 hour under an argon atmosphere (99.999%, Elme Messer), resulting in a material referred to as HT-Bat-res. To introduce nitrogen into the raw material or HT-Bat-res, we employed dicyandiamide (DCDA, Sigma-Aldrich, Germany) and polyvinylpyrrolidone (PVP, Sigma Aldrich, Germany, M_w: 40 000) in a ratio of 1 : 20 : 0.1, respectively. To obtain a homogeneous raw material : DCDA : PVP mixture in ethanol, 2 hours of sonication was applied. In the case of the heat-treated raw material, a mixture of HT-Bat-res : DCDA : PVP was subjected to ball milling (BM) for two rounds of 30 min each using 4 g of 0.5 mm ZrO_2 balls in a mixture of ethanol and water (2 : 1) as the medium. Subsequently, the dried mixtures were subjected to flash pyrolysis for 2 hours at 800 °C under an argon atmosphere, resulting in a catalyst known as Bat-res-N (N-doped raw material) or HT-Bat-res-BM-N (ball-milled and N-doped HT-Bat-res). An emphasis was placed on ensuring the repeatability of the synthesis process; therefore, at least three distinct syntheses per catalyst material were performed, and good repeatability was achieved.

Physical characterisation

Scanning electron microscopy (SEM, Mira 3, Tescan, Czech Republic) combined with an energy dispersive X-ray spectrometer (UltraDry Silicon Drift) and NSS microanalysis software (EDS, Thermo Fisher Scientific, USA) was used to analyse the surface morphology and bulk phase composition of the studied materials. The crystallinity and phase composition of these materials were analysed by powder X-ray diffraction (XRD) using a PANalytical X'Pert3 powder XRD instrument (CuKα radiation, λ = 1.54182 Å), with step size of 0.04° at 45 kV and 40 A. Raman spectra for the analysis of carbon structures of the materials were recorded using a confocal Raman microscope (Renishaw inViaTM, UK) with a 532 nm wavelength laser beam. Data analysis and fitting were performed by applying the Voigt function in the OriginPro (OriginLab Corporation, USA) program. N_2 adsorption–desorption analysis was used to determine the porosity and specific surface area at nitrogen boiling temperature (77 K). The specific surface area was measured by using the Brunauer–Emmett–Teller (BET) method and the pore size distribution was determined with DFT calculations. X-ray photoelectron spectroscopy (XPS) was carried out with a Kratos Axis Ultra spectrometer with monochromated Al Kα radiation using a pass energy of 40 eV, an X-ray power of 75 W and an analysis area of approximately 700 μm × 300 μm. The sp^2 carbon 1s peak at 284.5 eV was used as a charge reference. The elemental composition was determined from the peak areas of high-resolution core level spectra after Shirley background subtraction using equipment-specific sensitivity factors.

Electrochemical measurements

The ORR and the OER were studied with the rotating disk electrode (RDE) method using a Gamry potentiostat/galvanostat Interface 1010E instrument with a three-electrode system, where $Ag/AgCl_2$ (3 M KCl) was used as the reference electrode, a graphite rod was used as the counter electrode, and a 0.2 cm^2 glassy carbon (GC) electrode coated with the catalyst was used as the working electrode. An Origalys speed control unit and a rotator were used for the RDE method with rotation rates from 3600 to 400 rpm. The prepared catalyst ink has a concentration of 4 mg ml^{-1} in ethanol containing 1 μl $mg_{catalyst}{}^{-1}$ of 5 wt% Nafion™ solution. The suspension was previously sonicated for 1 h and, thereafter, 4 × 5 μl of catalyst ink was pipetted onto clean GC electrodes, resulting in 0.4 mg cm^{-2} catalyst loading. For easier comparison, all measured potentials were recalculated to values *vs.* reversible hydrogen electrode (RHE) by using the Nernst equation:

$$E(\mathrm{RHE}) = E_{\mathrm{Ag/AgCl}} + 0.059\,\mathrm{pH} + E^{\circ}_{\mathrm{Ag/AgCl}} \qquad (1)$$

where $E_{\mathrm{Ag/AgCl}}$ is the experimentally measured potential *vs.* Ag/AgCl and $E^{\circ}_{\mathrm{Ag/AgCl}} = 0.210\,\mathrm{V}$ at 25 °C. ORR measurements were performed in 0.1 M KOH solution at room temperature, saturated with O_2 (Elme Messer, 5.0), and the gas flow was held constant over the solution throughout the experiment. Experiments were controlled with Gamry Instruments Framework software. OER measurements were carried out in N_2 (Elme Messer, 5.0)-saturated 1 M KOH solution at room temperature and the gas flow was held constant over the solution throughout the experiment. The *iR*-drop was eliminated from the OER polarization curves by compensating each of them through *iR*-drop elimination with respect to the solution's ohmic resistance. The ohmic resistance was determined from the EIS data obtained in the frequency range of 100 kHz–1 Hz (with 10 mV modulation) at the open circuit potential. The resistance value was obtained from the Nyquist plot by determining the real part of the impedance when the imaginary part was zero. For electrocatalytic activity assessment, a minimum of three separate RDE measurements, each with three electrodes, were conducted for each synthesized catalyst material.

Zinc–air battery (ZAB) experiments were conducted by using a custom-made test cell. An air electrode with active surface area of 0.79 cm^2 consisting of a gas diffusion layer (GDL, Sigracet 28BC by SGLCarbon, Germany) and a catalyst layer coated on the GDL, with a final loading of 1 mg cm^{-2}, was used. Ti mesh was used as an air electrode current collector. For comparison, a commercial catalyst of 20% PtRu (1 : 1 ratio) on a carbon support (FuelCellstore, USA) was also used as an air electrode catalyst material. A 6 M KOH + 0.2 M $Zn(Ac)_2$ electrolyte and a polished Zn plate (1 mm, 99.9%) were used to complete the ZAB cell. All measurements were conducted at room temperature. A PGSTAT30 potentiostat/galvanostat (Metrohm Autolab, The Netherlands), controlled by the NOVA 2.1.5 program, was used to control the ZAB tests. Galvanostatic charge–discharge cycling curves were obtained using 30 min charge and 30 min discharge processes at a current density of 10 mA cm^{-2}. The specific energy density and capacity were obtained with a complete discharge test and calculated based on the mass of consumed Zn. At least three different ZAB cells were tested to evaluate the maximum discharge power density for each synthesized catalyst material.

Results and discussion

Physicochemical characterisation of the samples

The starting material in this research was black mass leach residue (Fig. 1a), primarily comprised of graphite. However, it

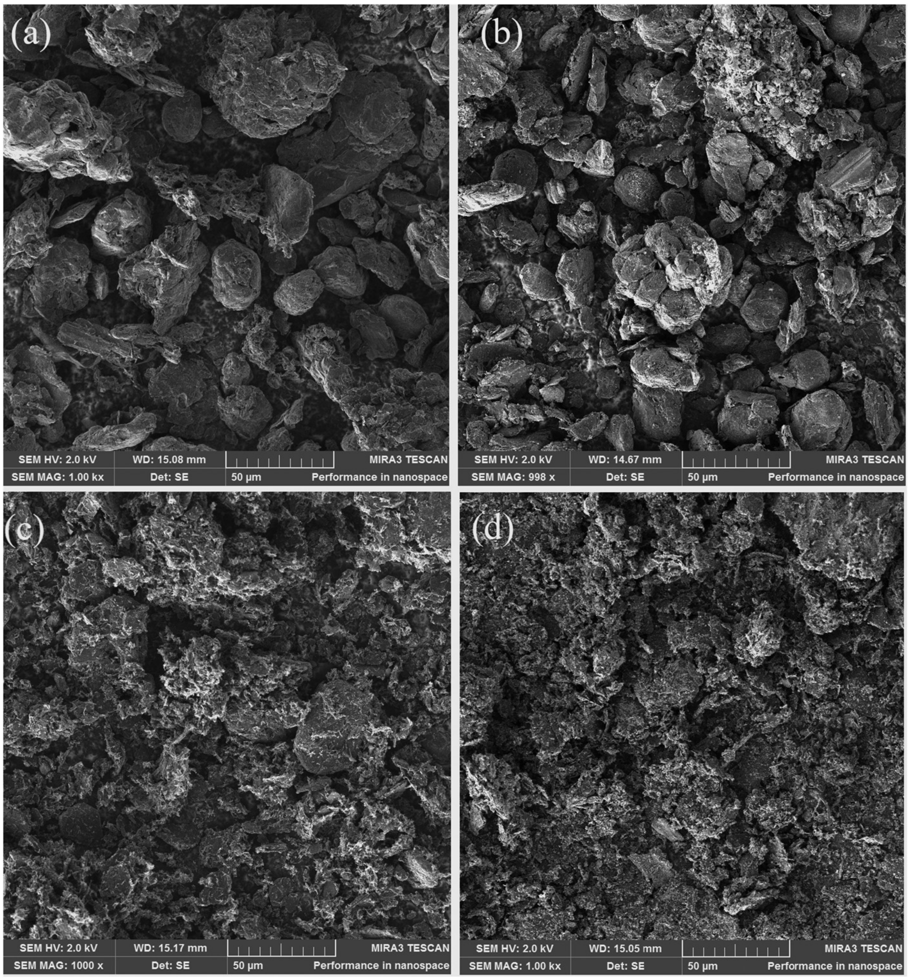

Fig. 1 SEM micrographs of (a) the raw material (black mass leach residue) and the (b) HT-Bat-res, (c) Bat-res-N and (d) HT-Bat-res-BM-N catalyst materials at 1000× magnification.

also contained remnants of other battery materials from the cathode (Co, Li, Mn, Ni), the current collectors (Cu and Al), and the binder material (PVDF, a source of F). These components were confirmed through SEM-EDX analysis (Table 1 and Fig. S1 in the ESI†) and XRD (Fig. S2†). The XRD diffractogram confirmed the presence of a high intensity peak at around 26.5° for graphite (ICDD: 96-901-1578). In addition, the residue contained $Li_{1.44}Co_3O_6$ (ICDD: 96-155-0393), $LiMn_2O_3$ (ICDD: 96-151-3968), SiO_2 (ICDD: 96-900-5033), Cu (ICDD: 96-901-2044), CoO (ICDD: 96-900-8619) and Al_2O_3 (ICDD: 00-010-0173), based on peaks in the XRD diffractogram. This is a typical composition for the black mass leach residue, which has traditionally been found to be very heterogeneous.[58,59] The heat treatment of leach residue successfully removed the PVDF, as demonstrated by the absence of elemental F in the treated materials, based on SEM-EDX mapping (Fig. S3† and Table 1). In addition, the results in Table 1 and Fig. S1, S3–S5† show that the relative concentrations of metals in the bulk increased with the heat treatment(s), showing the removal of organic phases. The removal of the binder played a role in breaking down the larger graphite chunks into smaller and more uniformly sized particles, as observed in Fig. 1a and b. Initially, the sizes of particles in the raw material were between 25 and 50 µm and exhibited a relatively roundish shape with a smooth surface (Fig. 1a). The introduction of nitrogen doping resulted in the development of compact and rough structures on the surface of the catalyst material, indicating the successful nitrogen doping of the graphite surface (as shown in Fig. 1c and d and Fig. S6†). In

Table 1 Elemental composition of the studied materials based on SEM-EDX mapping (Fig. S1†)

Element	Raw material (wt%)	HT-Bat-res (wt%)	Bat-res-N (wt%)	HT-Bat-res-BM-N (wt%)
C	79.6	82.88	80.77	75.84
O	15.05	13.43	15.33	18.63
Co	0.77	1.99	2.28	3.42
Mn	0.04	0.24	0.26	0.38
Ni	—	—	0.17	0.21
Al	0.39	0.39	0.46	0.45
Cu	0.43	0.52	0.51	0.49
F	3.05	—	—	—

the case of HT-Bat-res-BM-N, the ball-milling treatment led to a reduction in the size of the supporting graphite particles. In addition, these graphite particles appeared less roundish, instead displaying a flatter and thinner structure compared to the supporting material of the original raw material sample (Fig. S6†). XRD analyses of the pyrolyzed materials revealed that the undissolved active cathode material has undergone reduction, resulting in the formation of metal oxides and/or metallic species. These findings suggest that the graphite present in the leach residue can function as a reductive agent during the thermal treatment. Furthermore, in addition to graphite, it has been shown that aluminium in the presence of a carbon source can facilitate the thermal reduction of the cathode material.[60] Hu *et al.* have demonstrated that when subjected to higher temperature roasting in the presence of graphite, both Co and Ni exhibit a greater tendency for reduction into metallic species as compared to Mn, which predominantly remains in the oxide state at 900 °C.[61] Based on the transition metal traces, it was observed that Co exhibited the highest relative metal content (3.42%) in the HT-Bat-res-BM-N sample (Table 1). This finding suggests the potential formation of more stable Co–N–C active centres within the bulk of the material, which could enhance the stability of metallic Co.[62]

This observation was further corroborated by the XRD analysis (Fig. S7†), which revealed the disappearance of the CoO peak and a noticeable increase in the intensity of the Co(0) peak after N-doping. Subsequent to the heat treatment of the materials, distinct metallic Co (Co(0), ICDD: 96-901-1624) peaks became evident in the XRD patterns of the HT-Bat-res, Bat-res-N and HT-Bat-res-BM-N samples, indicating the successful decomposition of $Li_{1.44}Co_3O_6$. In the case of the Bat-res-N and HT-Bat-res-BM-N materials, the majority of Co existed in the Co(0) form, while for HT-Bat-res, Co was predominantly present as either Co_4O_4 or Co(0), as discerned from the XRD diffractograms. These results confirm that a substantial proportion of Co is reduced into its metallic form during the N-doping process, presumably integrated into the Co–N–C active centres within the material's bulk. Moreover, the diffractograms of Bat-res-N and HT-Bat-res-BM-N also indicate the presence of cobalt carbide ($C_{0.01}Co$, ICDD: 98-061-7394). The incorporation of Co nanoparticles into the carbon support material poses a significant challenge. However, it has been established that carbon nanotubes (CNTs) can form in the presence of cobalt nanoparticles and DCDA during the pyrolysis of carbon-based materials. The initiation of CNT growth on carbon is catalysed by metallic Co, which is often subsequently encapsulated within the CNTs. Our previous research has documented the growth of these CNTs under similar conditions.[58,63] In addition, XRD analysis identified Cu peaks (ICDD: 96-901-2044) in the diffractograms of the HT-Bat-res, Bat-res-N and HT-Bat-res-BM-N materials. The I_D/I_G ratio, determined from the Raman spectra (Fig. S8†) of the studied materials, revealed that with every process step, a higher graphitization rate and a lower surface defect level in the carbon lattice were achieved. It is important to note that the D-band intensity is influenced not only by vacancies and topological defects, but also by the presence of impurities.[64] It is believed that the removal of various impurities from the graphite fraction is the key factor in this work that influences the intensity of the D-band. The I_D/I_G ratio decreased from 0.72 to 0.50 with the removal of binder and organic phases. This effect can be attributed to the greater abundance of diverse oxygen groups that become attached to both the surface and edges of graphite following the acidic treatment (leaching) of the black mass. With N-doping of the samples, even lower I_D/I_G ratios were achieved, *i.e.* 0.40 and 0.28 for the Bat-res-N and HT-Bat-res-BM-N materials, respectively. These observations indicate that the introduction of N– and Co– into the carbon support material framework enhances the degree of graphitization, as corroborated by prior research that has been conducted. The introduction of graphitic nitrogen into the carbon framework after N-doping can contribute to the stabilization of graphitic planes in the carbon material, and thus promotes a more ordered and crystalline structure.[65] In addition, the cobalt and cobalt oxides present in the sample may also serve as catalysts for the transformation of amorphous carbon into graphitized carbon.[66] Furthermore, the combination of various treatment steps increased the specific surface area (S_{BET}) and porosity of the materials in the following order: raw material < HT-Bat-res < Bat-res-N < HT-Bat-res-BM-N, as shown in Fig. S9.† The removal of binder and organic phases from the leach residue increased the specific surface area from 2.4 to 9.9 $m^2\ g^{-1}$. Notably, ball milling of the HT-Bat-res material has a pronounced impact on the surface area of the HT-Bat-res-BM-N material, which reached 46.8 $m^2\ g^{-1}$. This outcome is favourable, as an increased surface area and porosity of the catalyst support material enhance mass transport within the material and introduce additional defects on the carbon surface. These defects can serve as anchoring sites for N– and metal species.[14,38,42] In order to obtain further insights into the possible extent of N-doping of the graphite support material, XPS analysis of the Bat-res-N and HT-Bat-res-BM-N materials was performed. Carbon, oxygen, nitrogen, and various Li-ion battery metals (Co, Li, Mn, Ni, Al, and Cu) were found in the samples by XPS analysis. The atomic concentrations are given in Table S1.† Fig. 2 shows the obtained and deconvoluted carbon, nitrogen and cobalt spectra of the two samples. The C 1s spectrum consists of a main asymmetric peak at 284.5 eV, which can be assigned to the sp^2 carbon. At binding energies between 285 and 289 eV, there will be some additional contributions from other types of carbon–carbon, carbon–oxygen and carbon–nitrogen bonds,[67–69] and N-peak fitting results for Bat-res-N and HT-Bat-res-BM-N (fitting parameters shown[58]) are presented in Table 2. The difference in the N-doping level, 5.6 at% for Bat-res-N *vs.* 6.4 at% for HT-Bat-res-BM-N, agrees well with the conclusion that ball milling leads to a reduction in the graphite particle size, resulting in a higher specific surface area and a greater number of defects in the carbon lattice. The Co 2p spectra (Fig. 2c) have been fitted with two components: metallic Co and Co(II).[58] The Co(II) component can contain contributions from both the CoO and Co–N

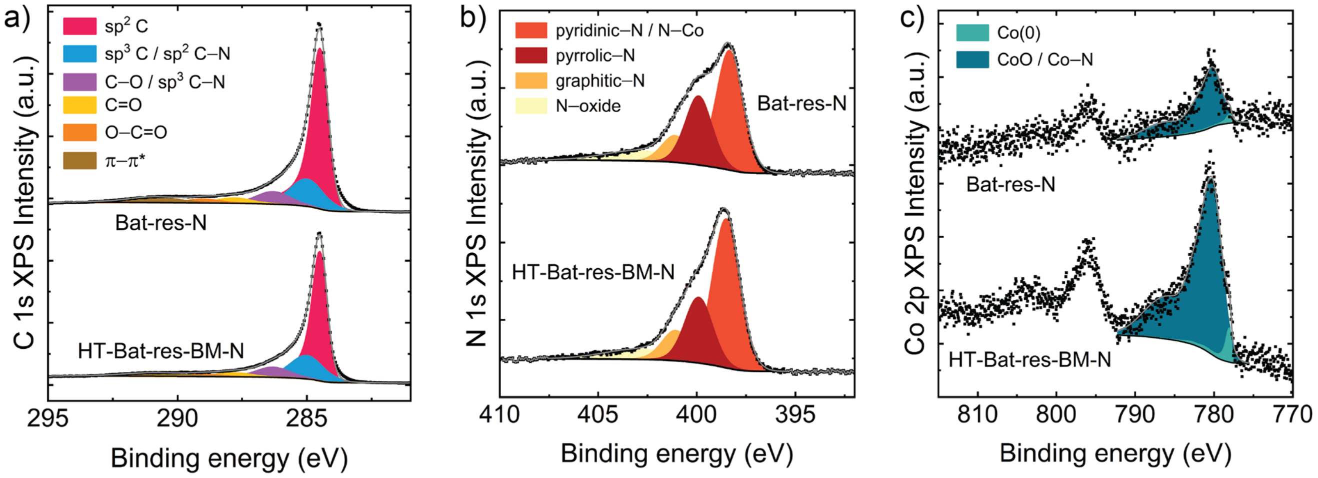

Fig. 2 X-ray photoelectron spectra of the Bat-res-N and HT-Bat-res-BM-N samples: (a) C 1s region, (b) N 1s region and (c) Co 2p region.

Table 2 N-peak fitting results based on XPS analysis (data from Fig. 2)

Name of the sample	Pyridinic N/N–Co	Pyrrolic N	Graphitic N	N oxide
Bat-res-N	50%	29%	11%	10%
HT-Bat-res-BM-N	55%	24%	11%	9%

bonds.[70,71] These defects provide more favourable sites for nitrogen groups to attach during the doping process. Pyridinic N, which is considered to be the most efficient nitrogen group for enhancing the ORR and OER,[72] has a concentration of 50% for the Bat-res-N catalyst and 55% for the HT-Bat-res-BM-N catalyst. The surface concentrations of Co were 0.1% and 0.4%, for Mn they were 0.5% and 0.9% and for Li they were 1.4% and 0.6%, respectively, for Bat-res-N and HT-Bat-res-BM-N. The concentration of battery metals on the catalyst surface, as determined through XPS analysis, exhibits a marked disparity compared to their concentration in the bulk of the studied materials, as determined from the EDX data. Concentrations are notably different especially for Co (0.4 at% *vs.* 3.42 wt%) and Al (2.1 at% *vs.* 0.45 wt%) in the case of the HT-Bat-res-BM-N sample. This variation in measurements is likely attributed to the inherent distinctions between the analysis methodologies. XPS captures data exclusively from the material's surface, penetrating to only a few atomic layers (typically up to 10 nm). In contrast, EDX analysis delves deeper, characterizing the material's bulk, with a penetration depth of approximately one μm. These findings suggest that the residues of Al, Mn, and Li are more prevalent on the surface of catalyst materials. In contrast, Co appears to be primarily integrated into the carbon support material, possibly forming bonds with active Co–N–C centres. This phenomenon could be related to the distinct reduction behaviours observed during the roasting process. It appears that Co undergoes reduction primarily to its metallic form, while other elements tend to remain in their oxide states, as discussed with respect to XRD analysis.

Electrocatalyst activity towards the ORR and OER

The modifications carried out on the black mass leach residue have increased its surface area and porosity, potentially leading to the formation of Co–N–C active centres that could promote the ORR and OER. The electrocatalytic activity of the synthesised materials as catalysts was first tested with regard to the ORR in 0.1 M KOH solution. The linear sweep voltammetry (LSV) curves and the determined electrochemical characteristics of the catalyst materials are presented in Fig. 3a and Table 3, respectively. The E_{onset} value increased with every following treatment step, showing that the N-doping of the material enhanced the electrochemical activity, with the highest values being for the Bat-res-N and HT-Bat-res-BM-N catalysts, at 0.875 V and 0.890 V, respectively. The half-wave potential ($E_{1/2}$) and limiting current density (j) of the HT-Bat-res-BM-N catalyst were 0.795 V and 4.81 mA cm^{-2}, respectively, demonstrating its excellent ORR performance. The formation of these active centres and the increased surface area were corroborated through a comprehensive analysis involving XRD, SEM-EDX, XPS and N_2 adsorption/desorption analyses. Notably, the HT-Bat-res-BM-N catalyst exhibited the highest specific surface area, a crucial attribute for enhancing the ORR because it allows for a greater capacity to host active centres.[38] The LSV polarization curves at different rotation rates for the Bat-res-N and HT-Bat-res-BM-N catalysts can be seen in Fig. S10a and S10b,† respectively. The Koutecky–Levich (K–L) plots (Fig. S10c and S10d†) were derived from the LSV curves. These plots exhibit a consistent linearity and parallelism across all the examined potentials, implying that the reaction is predominantly limited by mass transport. Based on the K–L plots, the number of electrons (n) transferred per O_2 molecule (Fig. S10b and S10d†) was calculated. The results indicated that the oxygen was reduced mainly *via* a $4e^-$ pathway, where O_2 is directly transformed into H_2O without forming intermediate H_2O_2.[73] The Tafel plots in Fig. S10e† show that the HT-Bat-Res-BM-N and Bat-res-N catalysts exhibit similar slopes of −52 mV dec^{-1} and −60 mV dec^{-1}, respectively. Remarkably,

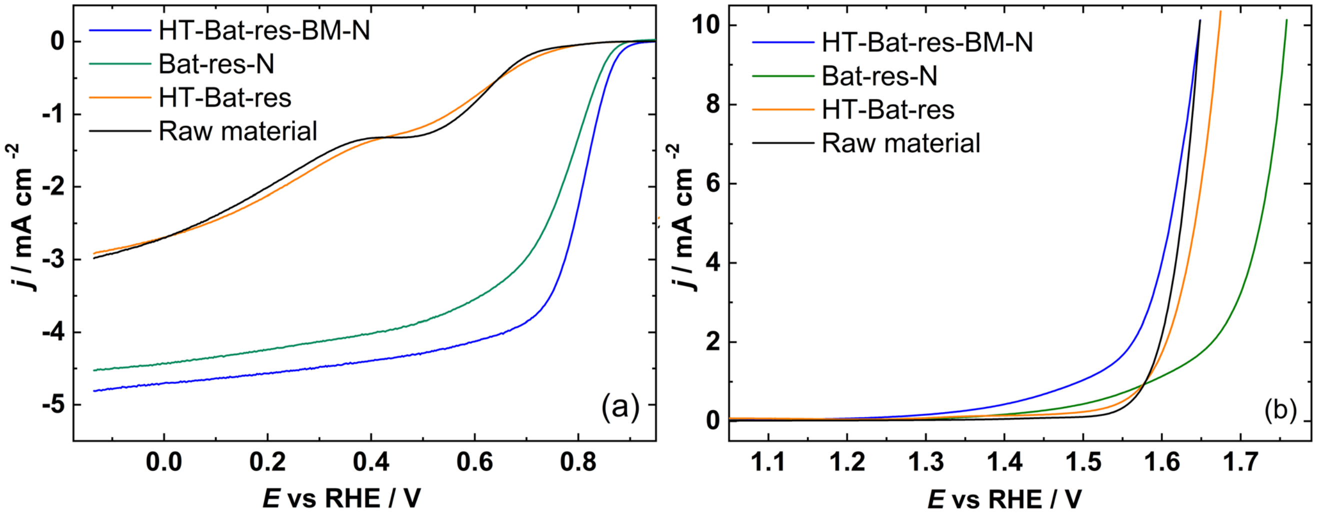

Fig. 3 RDE electrochemical characteristics of the studied materials: (a) ORR polarization curves at 1600 rpm in O_2-saturated 0.1 M KOH solution and (b) OER polarization curves at 1600 rpm in N_2-saturated 1 M KOH solution.

Table 3 Electrochemical characteristics of the raw material and different catalysts

Catalyst	ORR E_{onset} (V *vs.* RHE)	OER $E_{1/2}$ (V *vs.* RHE)	j (mA cm^{-2})	E (V)@ 10 mA cm^{-2}
Raw material	0.745	0.327	2.98	1.648
HT-Bat-res	0.767	0.370	2.92	1.675
Bat-res-N	0.875	0.755	4.53	1.759
HT-Bat-res-BM-N	0.890	0.795	4.81	1.648

these values align with those commonly observed for Pt-based catalysts. This suggests that the rate-determining step in the reaction mechanism is primarily associated with the initial reduction of O_2.[74] A comparison of the OER activity between the studied materials is shown in Fig. 3b and Table 3. Again, HT-Bat-res-BM-N showed the highest activity with E (V) @10 mA cm^{-2} = 1.648 V *vs.* RHE, while HT-Bat-res and Bat-res-N showed higher potentials of 1.675 V and 1.759 V *vs.* RHE. The untreated raw material also demonstrated good activity towards the OER with E (V)@10 mA cm^{-2} = 1.648 V *vs.* RHE, which can be attributed to traces of metal oxides in the bulk raw material. XRD analyses demonstrated the presence of Co_4O_4 in the raw material (Fig. S2†). Co_4O_4 implies a compound with a combination of cobalt atoms in different oxidation states, including cobalt(II) and cobalt(III). The presence of multiple oxidation states suggests a mixed valency, which tends to be effective in catalysing the OER.[75] The N-doped materials exhibit a Tafel slope (Fig. S10f†) of 140 mV dec^{-1} and 119 mV dec^{-1} for Bat-res-N and HT-Bat-res-BM-N, respectively, while the undoped materials exhibit Tafel slopes of 71 mV dec^{-1} (raw material) and 97 mV dec^{-1} (HT-Bat-res). The increase of Tafel slopes for the N-doped materials could indicate that mass transfer is the rate limiting step and the effective electrode surface area is lower.[40] HT-Bat-res-BM-N showed excellent activity and stability towards both the ORR and OER due to the formation of electrochemically active Co–N–C and Co(0) species. Multi-metal catalyst materials have good ORR/OER bifunctional electrocatalytic activity due to the synergistic effect of the metals, but the concrete effects of multi-metallic catalyst materials are still under debate.[49,50,76]

Performance as an air electrode catalyst in zinc–air batteries

To assess the synthesized catalyst's viability for end application, we constructed a zinc–air battery (ZAB) (Fig. S11a†). This allowed us to evaluate the catalyst's bifunctional performance when employed as an air cathode catalyst material. For comparison purposes, we also employed a commercial catalyst consisting of 20% PtRu/C as the air electrode catalyst material. All the studied catalyst materials showed very similar open circuit potential values (Fig. S11b†) of 1.40 V for HT-Bat-res-BM-N and 1.45 V for PtRu/C. The peak power density (Fig. 4a) for HT-Bat-res-BM-N was 104 mW cm^{-2} at a current density of 173 mA cm^{-2}, which is 32 mW higher than what was achieved with a 20% PtRu/C catalyst-based ZAB. By comparing the charging and discharging polarization curves of the catalysts, HT-Bat-res-BM-N has the higher discharge voltage; however, all catalyst materials have similar charge voltages, as can be seen from Fig. 4b. Complete discharge tests were carried out to calculate the specific capacity and energy of the constructed ZAB (Fig. 4c and Table 4). The highest specific capacity of 765 mA h g^{-1} was achieved with the HT-Bat-res-BM-N catalyst. Both the N-doped catalysts demonstrated higher power density than the raw material-based catalyst, showing the enhancement effects of nitrogen doping and the increased surface area, which provides a greater number of active centres for both the ORR and OER. The stability of the catalyst materials was tested during charge–discharge cycling at a current of 10 mA cm^{-2} with a 30 min charge and discharge time, as can be seen in Fig. 4d. The HT-Bat-res-BM-N catalyst showed outstanding stability up to 80 cycles with an average round-trip efficiency of 55% and a

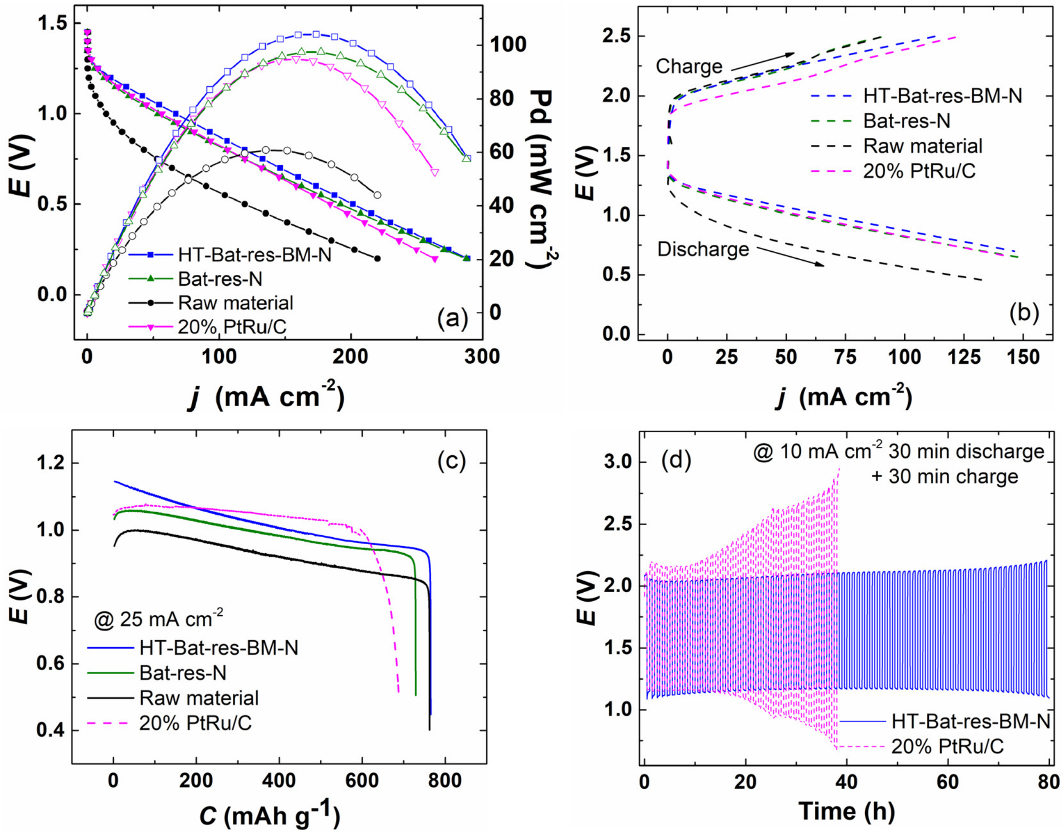

Fig. 4 ZAB results of the studied catalysts and the 20% PtRu/C catalyst: (a) discharge polarization curves and power density curves, (b) charge and discharge polarization curves, (c) complete discharge test, (d) galvanostatic charge/discharge cycling.

Table 4 Specific capacity and specific energy of the studied catalysts and PtRu/C

Name of the sample	Raw material	Bat-res-N	HT-Bat-res-BM-N	20% PtRu/C
Specific capacity (mA h g^{-1})	762	729	765	688
Specific energy (W h kg^{-1})	705	723	780	705

voltage gap of 0.95 V. In contrast, 20% PtRu/C showed an initially higher round-trip efficiency (60%) and a smaller voltage gap (0.79 V), but its performance started to decrease quickly after 10 potential cycles showing the superior cycling stability and efficiency of the HT-Bat-res-BM-N catalyst.

The performance and stability of HT-Bat-res-BM-N do not currently surpass those of the top catalysts employed in ZABs.[38,42,46,47,51,53] However, it is important to note that all these reference catalysts were synthesized using costly and precious pure materials and complicated synthesis routes. Table S2† provides a comparative overview of bi- or trimetallic bifunctional N-doped carbon catalysts for ZABs.

The catalysts developed in this research offer a significant advantage, as they are synthesized from industrial recycling waste, facilitating the responsible and sustainable use of critical resources. Furthermore, this approach introduces an innovative, straightforward, and economically efficient method for repurposing waste graphite derived from LIBs.

Conclusions

In this study, we revealed the undiscovered potential of the Li-ion battery black mass leach residue, typically discarded as industrial hydrometallurgical recycling waste, as a valuable raw material for synthesis of electrocatalytically active bifunctional oxygen electrocatalysts. By taking advantage of the metal impurities present in the black mass leach residue, we incorporated nitrogen and Co into the graphite support material through a ball milling and pyrolysis modification process. The resulting material, HT-Bat-res-BM-N, exhibited high electrocatalytic activity for both the ORR and OER.

This remarkable performance can be attributed to the development of electrocatalytically active nitrogen and cobalt centres, as well as an increased surface area compared to that of the original material. We further assessed the applicability of these battery waste-derived catalysts by employing them as air electrode catalyst materials in a zinc–air battery. HT-Bat-res-BM-N demonstrated an impressive power density of 104 mW cm^{-2} and outstanding stability, withstanding

80 hours of charge–discharge cycling at 10 mA cm^{-2}. Notably, it outperformed the commercial 20% PtRu/C catalyst in this application. This research highlights the previously undiscovered value of the Li-ion battery leach residue as a valuable resource for the preparation of transition metal-doped carbon-based materials, which holds great promise for enhancing energy conversion and storage devices. The catalysts developed in this research provide notable advantages by utilizing industrial recycling waste and promoting responsible resource use. In addition, this approach presents an innovative, cost-effective method for repurposing waste graphite from LIBs.

Author contributions

R. P.: conceptualization, investigation, and writing – original draft. A. C.: investigation (SEM-EDX and Raman) and writing – original draft. J. S.: investigation (XPS) and writing – original draft. M. L.: resources and writing – original draft. I. K.: resources, supervision, and writing – original draft. K. L.: conceptualization, funding acquisition, investigation, project administration, and writing – original draft.

Conflicts of interest

The authors declare that there are no conflicts of interest.

Acknowledgements

This research was supported by the Estonian Research Council (PSG312, PSG926, EAG248), the Environmental Investment Centre (KIK 17988), and the Business Finland BatCircle2.0 project (Grant Number 44886/31/2020). Additionally, the Academy of Finland's RawMatTERS Finland Infrastructure (RAMI) based at Aalto University and the OtaNano – Nanomicroscopy Center (Aalto-NMC) were utilized as part of this research.

References

1 IEA, *The Role of Critical Minerals in Clean Energy Transitions*, Paris, 2021.
2 H. E. Melin, *The Lithium-Ion Battery Life Cycle Report*, London, 2021.
3 O. Velázquez-Martínez, J. Valio, A. Santasalo-Aarnio, M. Reuter and R. Serna-Guerrero, *Batteries*, 2019, **5**, 68.
4 S. Natarajan, M. L. Divya and V. Aravindan, *J. Energy Chem.*, 2022, **71**, 351–369.
5 European Commission, *Critical Raw Materials Resilience: Charting a Path towards greater Security and Sustainability*, European Commission, Brussels, 2020.
6 U.S. Geological Survey, *2022 Final List of Critical Minerals*, Reston, VA, 2022.
7 A. D. Jara, A. Betemariam, G. Woldetinsae and J. Y. Kim, *Int. J. Min. Sci. Technol.*, 2019, **29**, 671–689.
8 J. Neumann, M. Petranikova, M. Meeus, J. D. Gamarra, R. Younesi, M. Winter and S. Nowak, *Adv. Energy Mater.*, 2022, **12**, 2102917.
9 A. Chernyaev, J. Partinen, L. Klemettinen, B. P. Wilson, A. Jokilaakso and M. Lundström, *Hydrometallurgy*, 2021, **203**, 105608.
10 M. Abdollahifar, S. Doose, H. Cavers and A. Kwade, *Adv. Mater. Technol.*, 2022, 2200368.
11 J. Liu, H. Shi, X. Hu, Y. Geng, L. Yang, P. Shao and X. Luo, *Sci. Total Environ.*, 2022, **816**, 151621.
12 Q. Cheng, Y. Han, Y. You, C. Hou, P. Perumal, B. Raj, M. Mohapatra and S. Basu, *JPhys Energy*, 2022, **4**, 045003.
13 H. Wang, Y. Huang, C. Huang, X. Wang, K. Wang, H. Chen, S. Liu, Y. Wu, K. Xu and W. Li, *Electrochim. Acta*, 2019, **313**, 423–431.
14 K. Liivand, M. Kazemi, P. Walke, V. Mikli, M. Uibu, D. D. Macdonald and I. Kruusenberg, *ChemSusChem*, 2021, **14**, 1103–1111.
15 W. Fang, J. Zhao, W. Zhang, P. Chen, Z. Bai and M. Wu, *J. Alloys Compd.*, 2021, **869**, 158918.
16 J. Sun, N. Wang, Z. Qiu, L. Xing and L. Du, *Catalysts*, 2022, **12**, 843.
17 I. Staffell, D. Scamman, A. Velazquez Abad, P. Balcombe, P. E. Dodds, P. Ekins, N. Shah and K. R. Ward, *Energy Environ. Sci.*, 2019, **12**, 463–491.
18 H. J. Kim, H. Y. Kim, J. Joo, S. H. Joo, J. S. Lim, J. Lee, H. Huang, M. Shao, J. Hu, J. Y. Kim, B. J. Min, S. W. Lee, M. Kang, K. Lee, S. Choi, Y. Park, Y. Wang, J. Li, Z. Zhang, J. Ma and S. Il Choi, *J. Mater. Chem. A*, 2021, **10**, 50–88.
19 S. Ghosh and R. N. Basu, *Nanoscale*, 2018, **10**, 11241–11280.
20 X. X. Wang, M. T. Swihart and G. Wu, *Nat. Catal.*, 2019, **2**, 578–589.
21 Z. Liang, H. Zheng and R. Cao, *Sustainable Energy Fuels*, 2020, **4**, 3848–3870.
22 B. Mohanty, P. Bhanja and B. K. Jena, *Mater. Today Energy*, 2022, **23**, 100902.
23 Y. J. Wu, X. H. Wu, T. X. Tu, P. F. Zhang, J. T. Li, Y. Zhou, L. Huang and S. G. Sun, *Appl. Catal., B*, 2020, **278**, 119259.
24 F. Yu, Q. Ying, S. Ni, C. Li, D. Xue and Y. Yang, *Dalton Trans.*, 2021, **50**, 16185–16190.
25 C. Zhu, Q. Shi, B. Z. Xu, S. Fu, G. Wan, C. Yang, S. Yao, J. Song, H. Zhou, D. Du, S. P. Beckman, D. Su and Y. Lin, *Adv. Energy Mater.*, 2018, **8**, 1801956.
26 J. Zhang, Z. Xia and L. Dai, *Sci. Adv.*, 2015, **1**, 1500564.
27 T. W. Chen, G. Anushya, S. M. Chen, P. Kalimuthu, V. Mariyappan, P. Gajendran and R. Ramachandran, *Materials*, 2022, **15**, 458.
28 H. Pourfarzad, M. Shabani-Nooshabadi and M. R. Ganjali, *J. Power Sources*, 2020, **451**, 227768.
29 R. Jasinski, *Nature*, 1964, **201**, 1212–1213.
30 H. Jahnke, M. Schönborn and G. Zimmermann, *Top. Curr. Chem.*, 1976, **61**, 133–181.
31 P. Bogdanoff, I. Herrmann, M. Hilgendorff, I. Dorbandt, S. Fiechter and H. Tributsch, *J. New Mater. Electrochem. Syst.*, 2004, **7**, 85–92.

32 B. Chi, X. Zhang, M. Liu, S. Jiang and S. Liao, *Prog. Nat. Sci.: Mater. Int.*, 2020, **30**, 807–814.

33 R. Praats, M. Käärik, A. Kikas, V. Kisand, J. Aruväli, P. Paiste, M. Merisalu, A. Sarapuu, J. Leis, V. Sammelselg, J. C. Douglin, D. R. Dekel and K. Tammeveski, *J. Solid State Electrochem.*, 2021, **25**, 57–71.

34 R. Praats, M. Käärik, A. Kikas, V. Kisand, J. Aruväli, P. Paiste, M. Merisalu, J. Leis, V. Sammelselg, J. H. Zagal, S. Holdcroft, N. Nakashima and K. Tammeveski, *Electrochim. Acta*, 2020, **334**, 135575.

35 S. Ratso, M. Käärik, M. Kook, P. Paiste, V. Kisand, S. Vlassov, J. Leis and K. Tammeveski, *ChemElectroChem*, 2018, **5**, 1827–1836.

36 S. Ratso, A. Zitolo, M. Käärik, M. Merisalu, A. Kikas, V. Kisand, M. Rähn, P. Paiste, J. Leis, V. Sammelselg, S. Holdcroft, F. Jaouen and K. Tammeveski, *Renewable Energy*, 2021, **167**, 800–810.

37 T. Liu, S. Cai, Z. Gao, S. Liu, H. Li, L. Chen, M. Li and H. Guo, *Electrochim. Acta*, 2020, **335**, 135647.

38 Z. Meng, N. Chen, S. Cai, R. Wang, W. Guo and H. Tang, *Int. J. Energy Res.*, 2021, **45**, 6250–6261.

39 T. Yu, H. Xu, Z. Jin, Y. Zhang and H.-J. Qiu, *Appl. Surf. Sci.*, 2023, **610**, 155624.

40 L. Negahdar, F. Zeng, S. Palkovits, C. Broicher and R. Palkovits, *ChemElectroChem*, 2019, **6**, 5588–5595.

41 Q. Qin, P. Li, L. Chen and X. Liu, *ACS Appl. Mater. Interfaces*, 2018, **10**, 39828–39838.

42 D. Wang, P. Yang, H. Xu, J. Ma, L. Du, G. X. Zhang, R. Li, Z. Jiang, Y. Li, J. Zhang and M. An, *J. Power Sources*, 2021, **485**, 229339.

43 L. Yang, D. Wang, Y. Lv and D. Cao, *Carbon*, 2019, **144**, 8–14.

44 X. Wan, X. Guo, M. Duan, J. Shi, S. Liu, J. Zhang, Y. Liu, X. Zheng and Q. Kong, *Electrochim. Acta*, 2021, **394**, 139135.

45 H. Luo, W.-J. Jiang, S. Niu, X. Zhang, Y. Zhang, L.-P. Yuan, C. He, J.-S. Hu, H. Luo, C. He, W. Jiang, S. Niu, X. Zhang, Y. Zhang, L. Yuan and J. Hu, *Small*, 2020, **16**, 2001171.

46 B. Lv, S. Zeng, W. Yang, J. Qiao, C. Zhang, C. Zhu, M. Chen, J. Di and Q. Li, *J. Energy Chem.*, 2019, **38**, 170–176.

47 R. Wang, H. Yang, N. Lu, S. Lei, D. Jia, Z. Wang, Z. Liu, X. Wu, H. Zheng, S. Ali, F. Ma and S. Peng, *J. Chem. Eng.*, 2022, **433**, 134500.

48 R. Wang, J. Cao, S. Cai, X. Yan, J. Li, W. M. Yourey, W. Tong and H. Tang, *ACS Appl. Energy Mater.*, 2018, **1**, 1060–1068.

49 K. Kisand, A. Sarapuu, A. Kikas, V. Kisand, M. Rähn, A. Treshchalov, M. Käärik, H.-M. Piirsoo, J. Aruväli, P. Paiste, J. Leis, V. Sammelselg, A. Tamm and K. Tammeveski, *Electrochem. Commun.*, 2021, **124**, 106932.

50 D. M. Morales, M. A. Kazakova, S. Dieckhöfer, A. G. Selyutin, G. V. Golubtsov, W. Schuhmann and J. Masa, *Adv. Funct. Mater.*, 2020, **30**, 1905992.

51 R. Hao, J. Chen, Z. Wang, Y. Huang, P. Liu, J. Yan, K. Liu, C. Liu and Z. Lu, *J. Colloid Interface Sci.*, 2021, **586**, 621–629.

52 S. Guo, J. Hu, S. Luo, Y. Zhang, Z. Zhang, P. Dong, X. Zeng, M. Xu, L. Han, J. Yuan, C. Zhang and Y. Zhang, *Int. J. Hydrogen Energy*, 2022, **47**, 8348–8358.

53 M. Zhang, X. M. Hu, Y. Xin, L. Wang, Z. Zhou, L. Yang, J. Jiang and D. Zhang, *Sep. Purif. Technol.*, 2023, **308**, 122974.

54 C. Yang, Z. Jin, X. Zhang, X. Zheng and X. He, *ChemElectroChem*, 2022, **9**, e202101494.

55 H. Bian, W. Wu, Y. Zhu, C. H. Tsang, Y. Cao, J. Xu, X. Liao, Z. Lu, X. Y. Lu, C. Liu and Z. Zhang, *ACS Sustainable Chem. Eng.*, 2023, **11**, 670–678.

56 K. S. Bejigo, S. Natarajan, K. Bhunia, V. Elumalai and S. J. Kim, *J. Cleaner Prod.*, 2023, **384**, 135520.

57 D. Ruan, K. Zou, K. Du, F. Wang, L. Wu, Z. Zhang, X. Wu and G. Hu, *ChemCatChem*, 2021, **13**, 2025–2033.

58 K. Liivand, J. Sainio, B. P. Wilson, I. Kruusenberg and M. Lundström, *Appl. Catal., B*, 2023, **332**, 122767.

59 A. Chernyaev, J. Partinen, L. Klemettinen, B. P. Wilson, A. Jokilaakso and M. Lundström, *Hydrometallurgy*, 2021, **203**, 105608.

60 S. Ma, F. Liu, K. Li, Z. Chen, F. Chen, J. Wang, S. Zhong, B. P. Wilson and M. Lundström, *Hydrometallurgy*, 2022, **213**, 105941.

61 J. Hu, J. Zhang, H. Li, Y. Chen and C. Wang, *J. Power Sources*, 2017, **351**, 192–199.

62 D. Lyu, Y. Du, S. Huang, B. Y. Mollamahale, X. Zhang, S. W. Hasan, F. Yu, S. Wang, Z. Q. Tian and P. K. Shen, *ACS Appl. Mater. Interfaces*, 2019, **11**, 39809–39819.

63 M. Kazemi, K. Liivand, M. Prato, P. Vacek, J. Walmsley, S. Dante, G. Divitini and I. Kruusenberg, *Energy Fuels*, 2023, **38**, 659–670.

64 P. T. Araujo, M. Terrones and M. S. Dresselhaus, *Mater. Today*, 2012, **15**, 98–109.

65 J. Liang and Q. Yuan, *Appl. Surf. Sci.*, 2024, **648**, 159025.

66 S. S. Li, J. K. Wang, Q. Zhu, X. W. Zhao and H. J. Zhang, *Solid State Phenom.*, 2018, **281**, 807–812.

67 T. I. T. Okpalugo, P. Papakonstantinou, H. Murphy, J. McLaughlin and N. M. D. Brown, *Carbon*, 2005, **43**, 153–161.

68 NIST X-ray Photoelectron Spectroscopy (XPS) Database Number 20, Gaithersburg MD, 2000.

69 A. Kousar, I. Pande, L. F. Pascual, E. Peltola, J. Sainio and T. Laurila, *Anal. Chem.*, 2023, **95**, 2983–2991.

70 Y. Wang, Y. Nie, W. Ding, S. G. Chen, K. Xiong, X. Q. Qi, Y. Zhang, J. Wang and Z. D. Wei, *Chem. Commun.*, 2015, **51**, 8942–8945.

71 Y. Yao, H. Chen, C. Lian, F. Wei, D. Zhang, G. Wu, B. Chen and S. Wang, *J. Hazard. Mater.*, 2016, **314**, 129–139.

72 H. Jiang, J. Gu, X. Zheng, M. Liu, X. Qiu, L. Wang, W. Li, Z. Chen, X. Ji and J. Li, *Energy Environ. Sci.*, 2019, **12**, 322–333.

73 H. T. Larijani and M. Khorshidian, *Appl. Surf. Sci.*, 2019, **492**, 826–842.

74 A. Holewinski and S. Linic, *J. Electrochem. Soc.*, 2012, **159**, H864–H870.

75 X. Zhao, F. Li, R. Wang, J. M. Seo, H. J. Choi, S. M. Jung, J. Mahmood, I. Y. Jeon and J. B. Baek, *Adv. Funct. Mater.*, 2017, **27**, 1605717.

76 A. Sajeev, A. Sathyaseelan, K. Serbara Bejigo and S. Jae Kim, *J. Colloid Interface Sci.*, 2023, **637**, 363–371.